

HIERARCHICAL INTEGRATED SPATIAL PROCESS MODELING OF MONOTONE WEST ANTARCTIC SNOW DENSITY CURVES

BY PHILIP A. WHITE¹, DURBAN G. KEELER^{2,*} AND SUMMER RUPPER^{2,†}

¹*Department of Statistics, Brigham Young University, pwhite@stat.byu.edu*

²*Department of Geography, University of Utah, *durban.keeler@gmail.com; †summer.rupper@geog.utah.edu*

Snow density estimates below the surface, used with airplane-acquired ice-penetrating radar measurements, give a site-specific history of snow water accumulation. Because it is infeasible to drill snow cores across all of Antarctica to measure snow density and because it is critical to understand how climatic changes are affecting the world's largest freshwater reservoir, we develop methods that enable snow density estimation with uncertainty in regions where snow cores have not been drilled.

In inland West Antarctica, snow density increases monotonically as a function of depth, except for possible microscale variability or measurement error, and it cannot exceed the density of ice. We present a novel class of integrated spatial process models that allow interpolation of monotone snow density curves. For computational feasibility we construct the space-depth process through kernel convolutions of log-Gaussian spatial processes. We discuss model comparison, model fitting and prediction. Using this model, we extend estimates of snow density beyond the depth of the original core and estimate snow density curves where snow cores have not been drilled. Along flight lines with ice-penetrating radar, we use interpolated snow density curves to estimate recent water accumulation and find predominantly decreasing water accumulation over recent decades.

1. Introduction. Antarctic snow density is directly linked with climate drivers and ice sheet dynamics. Snow density measurements are also used in combination with airplane radar measurements to estimate surface mass balance (SMB) over time (Medley et al. (2014)). As defined here, SMB is the net precipitation, sublimation, melt, refreeze and wind redistribution of snow and is directly linked to changes in climate. More accurate quantification of SMB greatly improves our understanding of net mass balance processes, provides a direct link to climate drivers of ice sheet mass balance and ice sheet dynamics and gives a reasonable target for climate and ice sheet process models. Because radar estimates of SMB require snow density measurements, accurate snow density estimation is essential. For this reason, researchers drill and analyze snow cores to measure snow density as a function of depth below the surface. However, snow cores often do not align with airplane flight lines with radar measurements.

Because the density of ice, which we call ρ_I , is 0.917 g/cm^3 , snow density can only take values between 0 g/cm^3 and ρ_I . Moreover, below the surface snow density generally increases as a function of depth, until it approaches the density of ice. Our goal here is to provide methods for estimating the snow depth-density curve in locations without drilled snow/ice cores while imposing appropriate functional constraints on our estimates of snow density. In this analysis we develop models for Antarctic snow density as a function of depth below the surface that allow for spatial interpolation. Using these models, we predict snow density against depth in locations without data. Within this framework that shares information from neighboring cores, we extend snow density estimates to deeper depths than were originally drilled.

Received August 2020; revised January 2021.

Key words and phrases. Bayesian statistics, Gaussian process, monotonic regression, spatial statistics, spline.

There is a rich literature on monotonic or isotonic function estimation or regression (see Barlow et al. (1972), Robertson, Wright and Dykstra (1988) for early discussion). This topic has been furthered under various modeling frameworks. In the frequentist literature these examples include splines (Ramsay (1988)) and restricted kernels (Müller and Schmitt (1988)). In a Bayesian framework, Gelfand and Kuo (1991) and Neelon and Dunson (2004) impose monotonicity through the prior distribution. More recently, Riihimäki and Vehtari (2010) propose monotonic curve estimation through constrained Gaussian processes (GP). Similarly, Lin and Dunson (2014) use Gaussian process projections to estimate monotone curves.

Building on differential equation models for snow densification, we propose a class of novel monotone spatial processes constructed by integrating over positive space-depth processes with respect to depth, yielding a spatial process of monotone increasing functions. We call this class of models monotone integrated spatial processes (MISPs). Given the size and attributes of our dataset (discussed in Section 2.2), we choose to construct the positive space-depth process through kernel convolutions of log-Gaussian spatial processes (see Higdon (1998, 2002) for early discussion on process convolution models for spatial modeling). We compare the performance of various kernels, including Gaussian, t , asymmetric Laplace and M-spline basis functions (Meyer (2008), Ramsay (1988)). As long as the kernel is amenable to integration, we can represent the model as a constrained spatially varying coefficient model with integrated kernels as predictors (Gelfand et al. (2003)). This model provides simple spatial prediction of snow density curves by model-based interpolation of basis function coefficients.

We highlight three additional contributions motivated by this dataset. Because snow density can only take values between 0 g/cm^3 and ρ_I , we model these spatially-varying monotone curves in a unique hierarchical generalized linear model framework that corresponds to commonly used constrained differential equations for snow densification (see, e.g., Herron and Langway (1980), Hörhold et al. (2011), Verjans et al. (2020)). In contrast to these common approaches, our approach allows this density curve to change its attributes to vary spatially. Snow density measurements are expected to be heteroscedastic because density measurements are taken as an average over some length of the core and are thus more certain when averaged over greater lengths. Moreover, the data come from four separate field campaigns, and, although their measurement methods are similar, we expect some differences in the measurement error associated with each group. To account for these patterns in variability, we consider models for the variance that account for the length of the core used for the measurement and allow model uncertainty to depend on the group that took the measurement. Lastly, we apply the approach of Keeler et al. (2020) to estimate SMB as a function of time, using snow density curve predictions at locations with airplane acquired radar measurements and providing a much richer recent history of water accumulation over the Antarctic ice sheets.

We continue this manuscript by discussing snow densification, including the differential equation framework that we adapt for our model and its relationship with surface mass balance in Section 2.1. We explore the snow density dataset that motivates our statistical contributions in Section 2.2 and comment briefly on the ice-penetrating radar data used to estimate SMB. Then, we present the class of integrated spatial process models in Section 3. Following our proposed methods, we give our final model for Antarctic snow density, including a discussion of our model comparison approach, model fitting and spatial interpolation in Section 4. We then analyze the results of our model in Section 5 and conclude our paper with final comments and a discussion of possible extensions in Section 6.

2. Snow density: Physics and data.

2.1. *Snow densification and surface mass balance.* Previous efforts to model the variation of snow density with depth take various forms, building upon the physics of densification (Cuffey and Paterson (2010)), empirical fits to data using exponential functions (Miège et al. (2013)) or a combination of the two (Herron and Langway (1980), Hörhold et al. (2011), Verjans et al. (2020), White et al. (2020)). The hybrid approach by Herron and Langway (1980) is the most widely used model. Changes in density ρ over depth x are generally modeled using a special case Bernoulli's differential equation,

$$(2.1) \quad \frac{d}{dx} \log\left(\frac{\rho}{\rho_I - \rho}\right) = z(x)$$

with solution, using integrating factors,

$$(2.2) \quad \log\left(\frac{\rho(x)}{\rho_I - \rho(x)}\right) = \alpha + \int_0^x z(t) dt,$$

$$\rho(x) = \rho_I \frac{e^{\alpha + \int_0^x z(t) dt}}{1 + e^{\alpha + \int_0^x z(t) dt}},$$

where α is a constant determined by the density at depth 0 and $z(x)$ is a positive function that varies over depth. In most literature (see, e.g., Herron and Langway (1980), Hörhold et al. (2011), Verjans et al. (2020)), $z(x)$ is modeled as a piecewise constant function. To represent the positive function of depth $z(x)$ more generally, we consider kernel convolutions of log-Gaussian spatial processes (LGPs) in Section 3.

Ice sheet surface mass balance (SMB) refers to the net sum of all changes in mass added to an ice sheet's surface within a given year, encompassing solid precipitation, melting/refreezing snow, blown snow and sublimation processes. Due to below freezing temperatures year-round and the relatively small fraction of sublimation in most regions (Lenaerts et al. (2012)), SMB in West Antarctica is reasonably approximated simply with falling and wind-blown snow. The classical method of measuring SMB in remote and extreme environments, like Antarctica, involves collecting ice cores, determining an age-depth scale using seasonal markers in snow/ice physical properties and chemistry and integrating snow/ice density over annual intervals to determine the total mass input (typically in water-equivalent depth) for a given year. These methods present some limitations, with low spatial coverage being one of the most important. Due to the extreme environments present in Antarctica, its lack of access and the expense of data collection, relatively few annually resolved records of SMB exist in West Antarctica with frequent clustering of coring sites. This sparsity, combined with the fact that point measurements at times are representative of only a few square kilometers (Banta et al. (2008), Eisen et al. (2008)), limits the applicability of conclusions drawn from ice core studies.

An important advancement to address this limitation is the use of ice-penetrating radar surveys to image internal layering in the snow subsurface, providing much-needed spatially distributed coverage of SMB estimates (Koenig et al. (2014)). This method, however, is unable to provide information about the depth-density relationship of the snow, and snow density information is needed to produce SMB estimates. This necessitates independent estimates of density to expand the utility of SMB radar methods.

We apply approaches from Keeler et al. (2020) to estimate surface mass balance in central West Antarctica over recent decades using estimates of snow density to 40 meters below the surface. This approach consists of computer vision algorithms, principally based on Radon transforms and peak finding, to pick annual snow layers in radar images to estimate annual

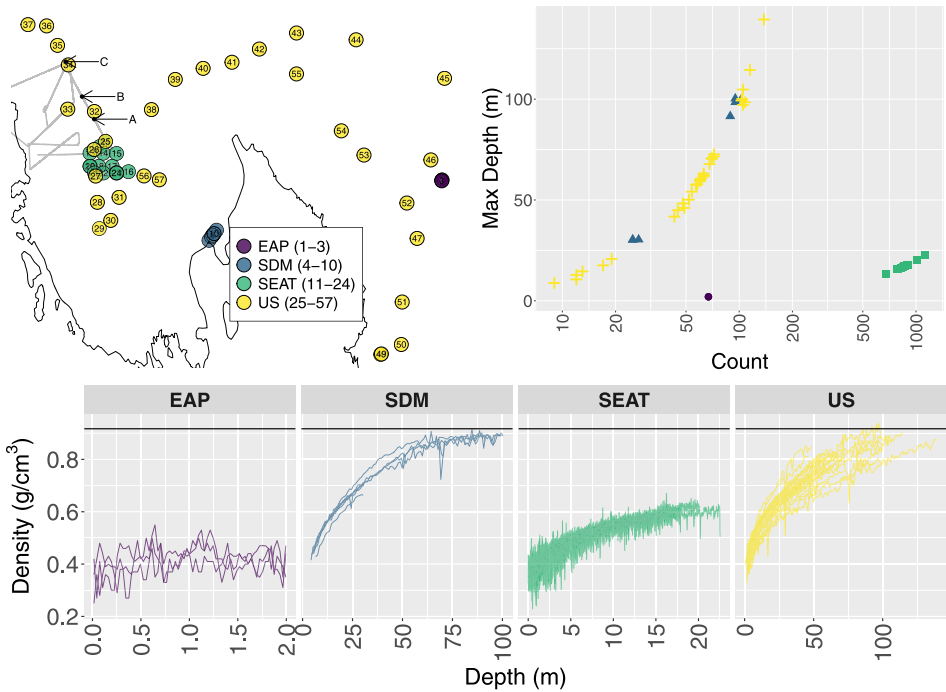


FIG. 1. (Top-Left) Location of core sites with colors indicating campaign. The gray line shows flight lines with ice-penetrating radar measurements, and arrows labeled with letters A, B and C, indicate sites where we illustrate snow density and SMB estimation. (Top-Right) Number of density measurements at each core plotted against core length (maximum depth) in m. (Bottom) Density measurements over depth by core, grouped by campaign. Note that the depth scales of these measurement types differ greatly. The black line indicates the density of solid ice.

SMB. The method first performs Radon transforms on iterative local subsections of an input echogram image, followed by a subroutine to identify peaks in the radar return strength of individual radar traces (typically corresponding to annual snow layers). These peaks are then grouped into laterally-continuous layers based on the integrated angle brightnesses determined in the Radon transform step and similarities in peak position, width and magnitude. Subsequent layers are assigned probabilities of representing annual layers based on layer length and return brightness. Monte Carlo simulations using these probabilities, combined with the depth-density profiles generated using the methods outlined in this paper, produce individual annual SMB distributions for each trace location in the radar image.

2.2. *Data.* Here, we discuss the data characteristics and constraints that influence our modeling decisions. Our dataset consists of 57 snow/ice cores at $n_s = 56$ locations, each with many density measurements. We index density measurements $\rho(s_i, x)$ by the core s_i , where s indicates the location and i indexes replication at site s and by depth x . We let \mathcal{S} denote the collection of core sites. The locations of the snow cores $s_i \in \mathcal{S}$, the flight lines with ground penetrating radar, the number of measurements in each core n_{s_i} , the length of the core x_{\max, s_i} and the measured density $\rho(s_i, x)$ as a function of depth are plotted in Figure 1. Most cores have between 20 and 1000 measurements, and, in total, the dataset contains $N = 14,844$ measurements.

These cores come from four field campaigns (indexed by $c(s_i)$), namely, the East Antarctic Plateau (Albert et al. (2004)), the Siple Dome project (Lamorey and Cooper (2002)), the Satellite Era Accumulation Traverse (Burgener et al. (2013)) and the U.S. portion of the International Trans-Antarctic Scientific Expedition (Mayewski et al. (2005)). In this paper we refer to these different campaigns as EAP, SDM, SEAT and U.S., respectively. As these

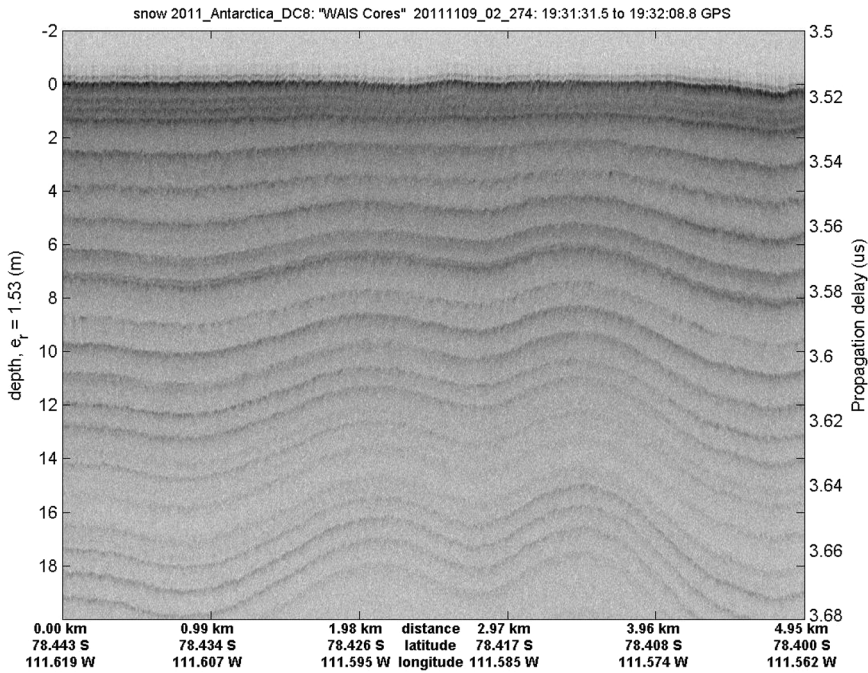


FIG. 2. Example of an ice-penetrating radar image. The visible layering represents seasonal variations in snow properties, causing reflections of radar pulses back to the transceiver. These annual layers, combined with snow depth-density estimates, are used to estimate annual SMB. Image from (Paden et al. (2019)).

projects were distinct undertakings, precise methods and techniques of density measurement differ somewhat between them, although most are similar.

The traditional and most commonly used method involves measuring the mass and volume of core sections. Density variability, however, relies not only on the mass and volume measurements themselves but also on the length of the core section used. Longer core sections smooth higher-frequency changes into a single bulk estimate, while increasingly small core sections better resolve short-term fluctuations. Density measurements made in the field are necessarily on long sections (typically one meter), while measurements performed in a lab are often over a few centimeters. The accuracy and precision of density measurements, therefore, depend on both the method and resolution of the measurements. Given the data attributes discussed, we consider combinations on variance models that account for: (1) the length of the core that is used to obtain that measurement and (2) the field campaign that obtained the density measurement.

Ice-penetrating radar permits nondestructive imaging of the snow sub-surface. Seasonal variations (in, e.g., air temperature, dust deposition, compaction rates, etc.) result in differences in the electromagnetic properties of snow deposited in summer compared to that in winter (Alley et al. (1990)). These contrasts act as reflection horizons for electromagnetic pulses sent from ground-based or airborne active radar systems (Fujita et al. (1999)). The combined reflected radar signals from repeated pulses of a moving radar system can, therefore, image the subsurface annual layering in Antarctic snow (see Figure 2).

3. Monotone integrated spatial process. In this section we present the class of monotone integrated spatial processes (MISP) for estimating monotone snow density curves. We define $z(\mathbf{s}, x) > 0$ to be a positive space-depth analog to $z(x)$ in (2.2). Using the integral of $z(\mathbf{s}, x)$, with respect to depth, we model the mean function of snow density $\mu(\mathbf{s}, x)$ as

$$(3.1) \quad \log\left(\frac{\mu(\mathbf{s}, x)}{\rho_I - \mu(\mathbf{s}, x)}\right) = w(\mathbf{s}, x) = \alpha(\mathbf{s}) + \int_0^x z(\mathbf{s}, t) dt.$$

This constrains the mean function $\mu(\mathbf{s}, x) \in (0, \rho_I)$ to be monotone increasing. To explore its properties here and in the Supplementary Material, we define $w(\mathbf{s}, x)$ to be the untransformed MISP. We clarify, however, that we only use $\mu(\mathbf{s}, x)$, a transformation of non-Gaussian processes, as the mean snow density.

As a brief aside, we mention a few of the mathematical properties of the MISP. Because $z(\mathbf{s}, x) > 0$, for any $x' > x$, we know $w(\mathbf{s}, x') > w(\mathbf{s}, x)$. That is, $w(\mathbf{s}, x)$ is monotone increasing as a function of x for any location \mathbf{s} . By standard real analysis, because $w(\mathbf{s}, x)$ is a monotone function over any interval $(0, T)$, it is differentiable almost everywhere on that interval by Lebesgue’s theorem for the differentiability of monotone functions. In addition to being differentiable almost everywhere, the covariance of $w(\mathbf{s}, x)$ is nonseparable and depth nonstationary, and there are explicit relationship between the mean and covariance (Hefley et al. (2017)) (see the online Supplementary Material White, Keeler and Rupper (2021)). Thus, this model provides a very flexible class of monotone functions.

To construct a positive space-depth process $z(\mathbf{s}, x)$, we use kernel convolutions (Higdon (1998, 2002)). The integrated space-depth function is

$$\begin{aligned}
 \int_0^x z(\mathbf{s}, t) dt &= \int_0^x \int_{\mathbb{R}} k(t - u) z^*(\mathbf{s}, u) du dt, \\
 (3.2) \qquad \qquad &= \int_{\mathbb{R}} \int_0^x k(t - u) z^*(\mathbf{s}, u) dt du, \\
 &= \int_{\mathbb{R}} (K(x - u) - K(0 - u)) z^*(\mathbf{s}, u) du,
 \end{aligned}$$

where $k(\cdot)$ is the smoothing kernel (a scaled PDF) with corresponding scaled CDF $K(\cdot)$ and $z^*(\mathbf{s}, u)$ is a spatial LGP for every depth u . Thus, our proposed method is a kernel convolution model using differences of CDFs as kernels. For computational feasibility with $N > 10^4$ and because the mean density function appears relatively smooth, we reduce the depth dimensionality of the space-depth process using process convolutions with a selection of depth-ordered knots $x_{\min} = 0 \leq \xi_1 \leq \dots \leq \xi_J \leq x_{\max} = \max_{\mathbf{s}_i} x_{\max, \mathbf{s}_i}$. However, we do not reduce dimensionality over space. In this framework we can express the space-depth random function $w(\mathbf{s}, x)$ as a linear model,

$$\begin{aligned}
 (3.3) \qquad w(\mathbf{s}, x) &= \alpha(\mathbf{s}) + \sum_{j=1}^J K_j(x) z_j^*(\mathbf{s}) \\
 &= \alpha(\mathbf{s}) + \mathbf{K}(x)^T \mathbf{z}^*(\mathbf{s}),
 \end{aligned}$$

where $K_j(x) = \int_0^x k_j(u - \xi_j) du$ and $k_j(\cdot)$ and $z_j^*(\mathbf{s})$ are kernels and independent spatial log-Gaussian processes associated with each knot ξ_j . The vectors $\mathbf{K}(x)$ and $\mathbf{z}^*(\mathbf{s})$ contain J elements of integrated kernels $K_j(x)$ and log-Gaussian process elements $z_j^*(\mathbf{s})$ for $j = 1, \dots, J$. Importantly, the kernels $k_j(\cdot)$ need not be symmetric, and there are potential computational benefits to using truncated kernels, as this induces sparseness in $\mathbf{K}(x)$.

To complete this model, we must specify several components: the number of knots J , the spatially-varying intercept $\alpha(\mathbf{s})$, the smoothing kernels $k_j(\cdot) > 0$ and the spatial log-Gaussian processes $z_j^*(\mathbf{s})$, $j = 1, \dots, J$. The properties of this space-depth model are determined by these selections. We consider specifying $k_j(\cdot)$ using Normal, t and Asymmetric Laplace probability distributions with full support (\mathbb{R}) as well as M-spline bases. M-spline bases are, in fact, probability densities, as they are scaled to integrate to one (Ramsay (1988)), and, when integrated, M-splines bases yield I-spline bases common to monotone regression. Thus, monotone I-splines models are a special case of (3.3) and induce sparseness in $\mathbf{K}(x)$. M-splines bases naturally induce sparseness, but using truncated probability distributions can

provide the same desirable sparseness in “big-data” settings. We discuss the M-spline basis function in more detail in the Supplementary Material. We make model selections based on out-of-sample predictive performance (see Section 4.1).

4. Methods and models.

4.1. *Model selection.* To compare different models, we carry out 19-fold cross-validation for each model considered because our data come from 57 snow cores, and, holding out three cores, each model fitting is a convenient choice. Our modeling goal is estimating the entire snow density function at locations without drilled snow cores. In our comparison, therefore, we weight predictive performance measures by the length of the core that each hold-out measurement represents. Our model comparison measures, therefore, correspond to approximated integrated error measures common to density or function estimation (see, e.g., [Fryer \(1976\)](#), [Marron and Wand \(1992\)](#)).

We let all model parameters be θ and use Markov chain Monte Carlo (MCMC) to obtain M posterior samples from the posterior distribution of θ . For each posterior sample $\theta^{(m)}$, $m = 1, \dots, M$, from our Markov chain Monte Carlo model fitting we generate a corresponding prediction $\rho^{(m)}(\mathbf{s}_i, x)$ for each hold-out observation $\rho(\mathbf{s}_i, x)$ from the posterior predictive distribution. We propose several criteria for comparing predictions to hold-out data: predictive squared and absolute error as well as a strictly proper scoring rule ([Gneiting and Raftery \(2007\)](#)), the continuous ranked probability score (CRPS) (see [Brown \(1974\)](#), [Matheson and Winkler \(1976\)](#), for early discussion on CRPS). We estimate CRPS using the empirical CDF of posterior predictions $\rho^{(m)}(\mathbf{s}_i, x)$ ([Krüger et al. \(2016\)](#)), which we denote $\text{CRPS}(\hat{F}(\mathbf{s}_i, x), \rho(\mathbf{s}_i, x))$,

$$(4.1) \quad \frac{1}{M} \sum_{j=1}^M |\rho^{(j)}(\mathbf{s}_i, x) - \rho(\mathbf{s}_i, x)| - \frac{1}{2M^2} \sum_{m=1}^M \sum_{m'=1}^M |\rho^{(m)}(\mathbf{s}_i, x) - \rho^{(m')}(\mathbf{s}_i, x)|,$$

where $\rho^{(m)}(\mathbf{s}_i, x)$ represents the m th sample from the posterior predictive distribution for core \mathbf{s}_i and depth x . Unlike squared or absolute error, which only use the posterior mean, CRPS compares the entire posterior predictive distribution to hold-out values and rewards predictive distributions concentrated on the correct value.

To define integrated squared and absolute errors, we use the maximum depth x_{\max, \mathbf{s}_i} of the core \mathbf{s}_i and number of measurements $n_{\mathbf{s}_i}$ at \mathbf{s}_i . We define integrated squared error (ISE) as

$$(4.2) \quad \sum_{\mathbf{s} \in \mathcal{S}} \sum_i \frac{x_{\max, \mathbf{s}_i}}{n_{\mathbf{s}_i}} \sum_x \left(\frac{1}{M} \sum_{m=1}^M \rho^{(m)}(\mathbf{s}_i, x) - \rho(\mathbf{s}_i, x) \right)^2.$$

Similarly, we defined integrated absolute error (IAE)

$$(4.3) \quad \sum_{\mathbf{s} \in \mathcal{S}} \sum_i \frac{x_{\max, \mathbf{s}_i}}{n_{\mathbf{s}_i}} \sum_x \left| \frac{1}{M} \sum_{m=1}^M \rho^{(m)}(\mathbf{s}_i, x) - \rho(\mathbf{s}_i, x) \right|.$$

We do not define an integrated (or weighted) CRPS because CRPS naturally incorporates model uncertainty (including weighting) probabilistically by accounting for the entire posterior predictive distribution.

We now present a summary of our model comparison, deferring a complete outline of the results to the Supplementary Material. The final model uses piecewise constant M-spline kernels $k_j(\cdot)$, corresponding to a linear I-spline, with five interior knots at five, 15, 30, 45 and 75 meters. To write this model as (3.3), we must include an additional knot at zero meters. The knot locations were chosen through model selection among a variety of knot selections.

These depth knots capture expected changes in densification patterns due to the interplay of particle rearrangement and plasticity changes at critical densities (Herron and Langway (1980), Hörhold et al. (2011)). The spatially-varying intercept $\alpha(\mathbf{s})$ and the log-Gaussian processes $z_j^*(\mathbf{s})$ are specified independently with exponential covariance using the great-circle distance, denoted $d(\mathbf{s}, \mathbf{s}')$, with shared spatial decay parameter ϕ and unique scale parameters σ_j^2 . The Gaussian process intercept and log-Gaussian process coefficients are centered on a unique scalar means. The mean function is nested within a truncated-Normal distribution with campaign-specific variance, scaled by the length of the core each measurement represents. The model is described in detail in Section 4.2 with prior distributions discussed in Section 4.3.

4.2. *Hierarchical model.* Here, we present the model for snow density with the best out-of-sample predictive performance. We constrain the mean function to lie between 0 g/cm³ and the density of ice ρ_I using a generalized logistic function with ρ_I as a maximum. Our hierarchical model for snow density is

$$\begin{aligned}
 \rho(\mathbf{s}_i, x) &\sim \mathcal{TN}\left(\mu(\mathbf{s}, x), \tau_{c(\mathbf{s}_i)}^2 \frac{n_{\mathbf{s}_i}}{x_{\max, \mathbf{s}_i}}, 0, \infty\right), \quad \rho(\mathbf{s}_i, x) > 0 \\
 \log\left(\frac{\mu(\mathbf{s}, x)}{\rho_I - \mu(\mathbf{s}, x)}\right) &= \alpha(\mathbf{s}) + \mathbf{K}(x)^T \mathbf{z}^*(\mathbf{s}), \quad \mu(\mathbf{s}_i, x) \in (0, \rho_I] \\
 \alpha(\mathbf{s}) &\sim \text{GP}(\gamma_0, \sigma_0^2 \exp(-\phi d(\mathbf{s}, \mathbf{s}'))), \quad \alpha(\mathbf{s}) \in \mathbb{R} \\
 z_j^*(\mathbf{s}) &\stackrel{\text{ind}}{\sim} \text{LGP}(\gamma_j, \sigma_j^2 \exp(-\phi d(\mathbf{s}, \mathbf{s}'))), \quad z_j^*(\mathbf{s}) > 0,
 \end{aligned}
 \tag{4.4}$$

where $\mathcal{TN}(\cdot, \cdot, 0, \infty)$ is a Gaussian error model truncated below by 0 using core-specific weights constructed with the maximum depth x_{\max, \mathbf{s}_i} and the number of density measurements $n_{\mathbf{s}_i}$, scaled by a campaign-specific scale parameter $\tau_{c(\mathbf{s}_i)}^2$. While the truncation is necessary to provide the proper support for $\rho(\mathbf{s}_i, x) > 0$, in practice, the truncation does very little because observations are not close to 0 g/cm³, given that estimated variances are small. Therefore, we refer to $\mu(\mathbf{s}, x)$ as a mean function rather than a location function. The GPs for $\alpha(\mathbf{s})$ and $\log(z_j(\mathbf{s}))$ are independent with shared decay parameter ϕ , unique scale parameters $\sigma_0^2, \dots, \sigma_6^2$ and location parameters $\gamma_0, \dots, \gamma_6$. Importantly, because each $z_j^*(\mathbf{s})$ is a log-Gaussian process, they each have a multiplicative rather than additive errors. Here, the mean of the model is a scaled inverse-logit transformation of a MISP using M-spline kernels with five interior knots (six knots in terms of (3.3) discussed in Sections 3 and 4.1). The mean function $\mu(\mathbf{s}, x)$ is not indexed by i because it does not depend on the core; however, the variance of the model is dependent on the core \mathbf{s}_i and the campaign $c(\mathbf{s}_i)$ that analyzed the core.

4.3. *Prior distributions, model fitting and interpolation.* To complete the model, we specify prior distributions for all model parameters. In this setting, standard mean-zero prior distributions for $\gamma_0, \dots, \gamma_6$ would suggest a model with high surface density and rapid snow densification. Our goal in selecting a prior distribution was choosing a model that would produce very flexible snow density estimates. Here, we assume the following prior distributions:

$$\begin{aligned}
 \gamma_0 &\sim \mathcal{N}(-0.5, 1), \quad \gamma_j \sim \mathcal{N}(-1.5, 1) \quad \text{for } j = 1, \dots, 6, \\
 \sigma_0^2 &\sim \mathcal{IG}(10, 3), \quad \sigma_j^2 \sim \mathcal{IG}(4, 3) \quad \text{for } j = 1, \dots, 6, \\
 \phi &\sim \text{Uniform}(10^{-5}, 10^{-1}), \quad \tau_{c(\mathbf{s}_i)}^2 \sim \text{Gamma}(1, 100) \quad \text{for all } c(\mathbf{s}_i),
 \end{aligned}
 \tag{4.5}$$

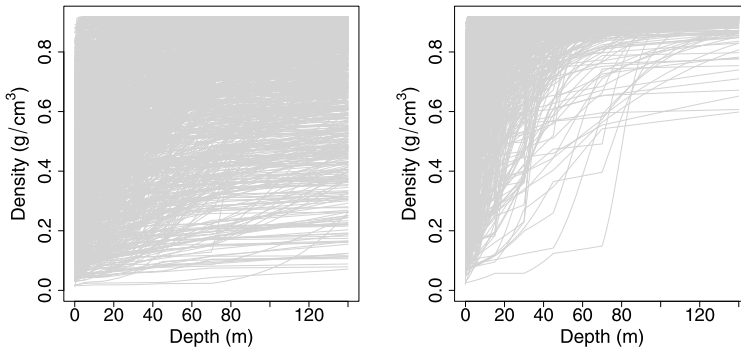


FIG. 3. Prior predicted mean snow density curves under (Left) our proposed model and (Right) zero-mean prior distributions.

where \mathcal{N} , $\mathcal{IG}(\cdot, \cdot)$ and Gamma are Normal, Inverse-Gamma and Gamma Distributions, respectively. Here, we use the parameterization of $\mathcal{IG}(a, b)$, indicating a mean $b/(a - 1)$ and $\text{Gamma}(a, b)$, that has expectation a/b .

Although these prior distributions are informative and nonstandard, we select them so that the mean prior surface density is between 0.35–0.4 g/cm³ and so that simulations from the prior distribution yield plausible and flexible snow density curves. In Figure 3 we plot 1000 realizations of the mean snow density simulated from our prior distribution and under a more standard, mean-zero model. Note that the zero-mean model generates informative and unrealistic density curves that put prior weight on near-ice density at shallow depths. Thus, our seemingly more informative prior is less informative and more realistic in the data space, while allowing great flexibility. We also highlight that there are several large jumps in the samples from the noninformative specification because the mean-zero normal random variables, when exponentiated, can be quite large and induce very rapid changes in the mean function. These changes in the function are particularly visible at knot locations. Lastly, we choose the prior distribution for ϕ , the common decay parameter for $\alpha(\mathbf{s})$ and $\log(z_j(\mathbf{s}))$, to be uniform between 10^{-5} and 10^{-1} to allow a wide range of possible values.

We sample from the posterior distribution, $\pi(\boldsymbol{\theta}|\boldsymbol{\rho})$, where $\boldsymbol{\rho}$ denotes all density measurements, using Hamiltonian Monte Carlo (HMC), implemented in Stan (Carpenter et al. (2017)). While several model parameters can be sampled in closed form using a Gibbs Sampler, the spatial random effects cannot, and using HMC improved the mixing of spatial random effects. Letting $\boldsymbol{\theta}$ be all model parameters, this model fitting approach yields M samples from the posterior distribution.

We use each of the posterior samples ($\boldsymbol{\theta}^{(1)}, \dots, \boldsymbol{\theta}^{(M)}$) to estimate snow density at hold-out locations and depths sampling from the posterior predictive distribution, via composition sampling (Tanner (1996)). That is, for every posterior sample $\boldsymbol{\theta}^{(m)}$, we simulate from the data model (4.4) to get posterior predictions for every hold-out $\rho(\mathbf{s}_i, x)$. When estimating snow densities at unobserved locations, however, we estimate $\mu(\mathbf{s}, x)$ rather than a noisy version of the mean. In conjunction with ice-penetrating radar measurements, estimated snow density curves can then be used to estimate a history of surface mass balance at that location using the methods discussed in Section 2.1, as we demonstrate in Section 5.

5. Results. Using Stan, we run our MCMC sampler for 55,000 iterations. We discard the first 5000 iterations, yielding 50,000 posterior samples on which we base our posterior inferences. In the Supplementary Material we demonstrate that the MCMC is well behaved. In total, this model fitting takes approximately 24 hours using one Intel(R) Xeon(R) Gold 6142 CPU @ 2.60 GHz processor.

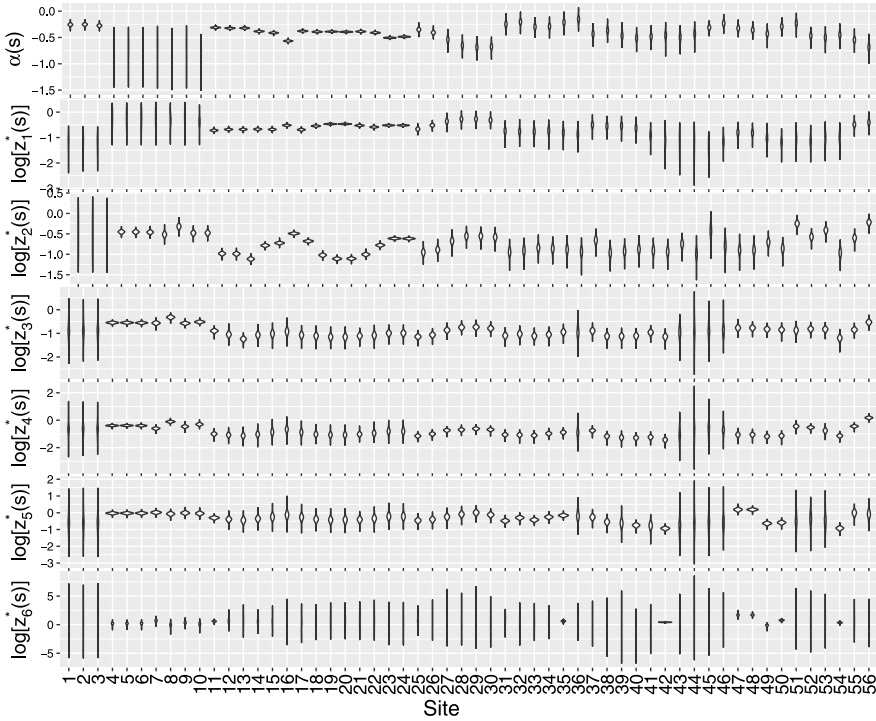


FIG. 4. Violin plots of posterior samples for all spatially-distributed random effects.

5.1. *Posterior summaries.* Based on 50,000 posterior samples, we provide violin plots for the posterior distributions for spatial terms, $\alpha(\mathbf{s})$ and $\log(z_j^*(\mathbf{s}))$, in Figure 4. We defer other posterior summaries to the Supplementary Material but note that the campaign-specific variances differ significantly, suggesting that these campaigns contributed different levels of noise to the data.

For some sites the posterior distributions are more diffuse, particularly for coefficients $(z_j^*(\mathbf{s}))$ that correspond to I-spline bases at greater depths. This generally happens when a snow core is shallow and does not extend past one or more of the interior knots. For example, the EAP cores are two-meter snow pits. For such cores, as discussed in Section 3, estimation of $\mathbf{z}^*(\mathbf{s})$ relies on information shared from nearby cores that have deeper observations. In addition, when the estimated snow density $\mu(\mathbf{s}, x)$ is close to ρ_I , even large changes in $z_j^*(\mathbf{s})$ may have little effect on $\mu(\mathbf{s}, x)$. For both of these reasons, estimates of $z_j^*(\mathbf{s})$ are generally more variable for larger j (see Figure 4).

The SDM cores, labeled 4–10, have lower and more uncertain estimated intercepts $\alpha(\mathbf{s})$ than other sites, meaning that the estimated surface density is lower relative to other sites. These cores are geographically and thus climatically isolated. For this reason it is unsurprising that they appear different than other cores, but these estimates are not incompatible with the estimates of other cores, cores 28–30, for example.

5.2. *Interpolation and extension of snow density curves.* In this section we show two utilities of this model: (1) extending snow density estimates beyond the depth of the original core and (2) estimating snow density curves at locations where snow cores have not been drilled. Both tasks are scientifically important, as the first task aids in studying a longer history of the Antarctic ice sheets while the second task allows us to estimate water accumulation in locations where we have not drilled snow cores.

For the first task we use cores 6, 24 and 42 (see Figure 1) as an illustration. Each core represents a unique scenario. Core 6 comes from a very tight cluster of deep snow cores from

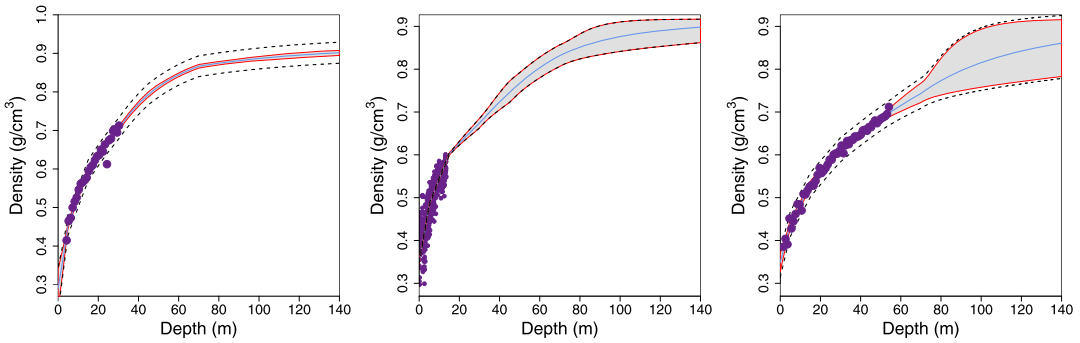


FIG. 5. Estimated snow density down to 140 m for (Left) Core 6, (Center) Core 24 and (Right) Core 42. The mean function is plotted in blue, 95% credible intervals on the mean as a polygon with red boundaries, 95% posterior prediction intervals in black dashed lines (using the correct campaign-specific scale parameter and assuming the same data spacing present in each core) and density measurements plotted as purple points.

the SDM project drilled near the coast with neighboring cores extending to nearly 100 meters that aid in precise estimation of snow densities at deeper depths. In coastal areas, densification generally occurs more rapidly due to slightly higher temperatures; therefore, there is a smaller difference between the density of ice and observed densities, making density estimates more precise. Core 24 is a 13.5 meter SEAT core in a data-rich area; however, in this region there are not many deep cores. Core 42 is a U.S. snow core that is slightly longer than 50 meters but is not in a relatively data-rich area. For each core we estimate the mean snow density $\mu(s, x)$ down to 140 meters (see Figure 5).

Because core 6 is near many deep cores, the estimated density curve is very precise, even though it only extends to 30 meters. The estimated snow density estimates for core 24 are very precise to about 40 m but become less certain at greater depths because neighboring cores lend less information at those depths. Compared to cores 6 and 24, core 42 lies in a data-poorer region with only four other cores within a 500 km range. Thus, our density estimates are much less certain beyond the range of measured density.

For the second task we estimate snow density along much of the flight line where ice-penetrating radar measurements were taken (see Figures 1 and 2). Due to low data quality at some locations, we were unable to obtain reliable SMB estimates. We estimate snow density down to 40 meters because, due to radar signal attenuation, these are the only densities useful for estimating SMB. Based on these snow density estimates along the flight line, we apply approaches from Keeler et al. (2020), briefly discussed in Section 2.1, to estimate SMB (with standard error) over recent decades. We focus on three locations without drilled snow cores, labeled “A,” “B” and “C” in Figure 1, to illustrate how estimated snow densities can be leveraged to estimate SMB (see Figure 6). Sites A and B show two of the most negative SMB trends (-14.1 and -12.2 mm w.e./yr., on average), while site C has one of the most positive estimated SMB trends, 0.7 mm w.e./yr. on average.

We plot the estimated SMB curves and time-averaged SMB estimates in Figure 7 along the flight line. Overall, we see lower SMB at latitudes closer to the south pole. For each estimated SMB curve, we estimate the trend over time using a weighted linear model and using the inverse squared standard error as weights. We plot the estimated trends in SMB in a histogram and at their locations on the flight line in Figure 8. Approximately 90% of the sites along these flight lines have estimated negative slopes. Overall, these results suggest generally negative trends in SMB across the central West Antarctic ice sheet. The preponderance of negative SMB trends is particularly noteworthy, as this region has experienced pronounced warming during the same time period (Bromwich et al. (2013)). As the moisture carrying capacity of air increases with temperature, the inverse relationship of SMB and air temperature in this

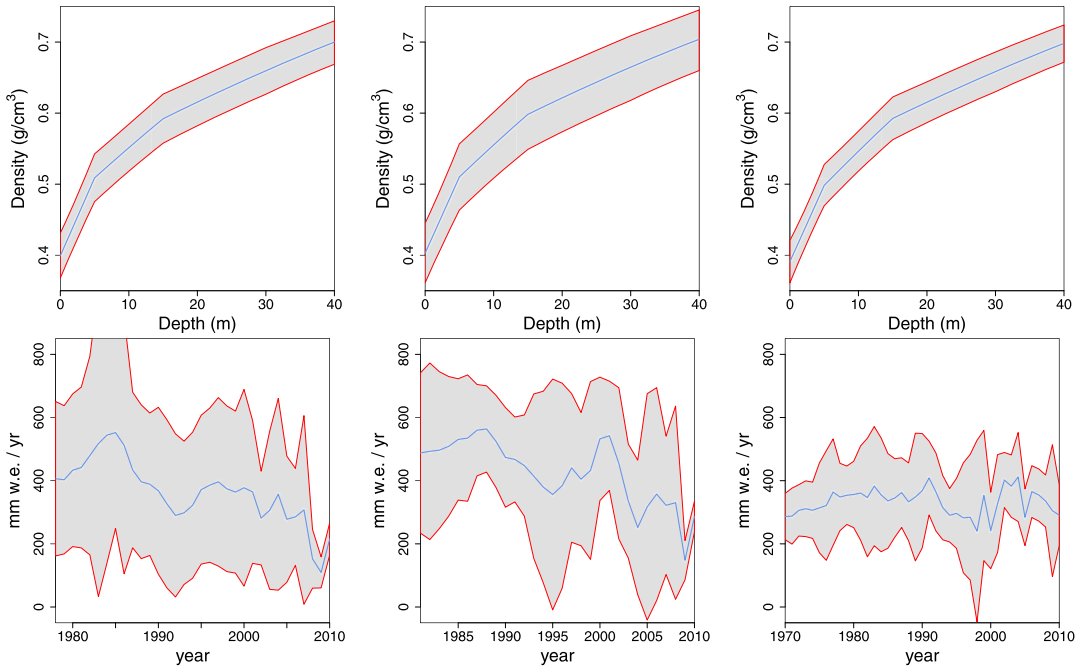


FIG. 6. (Top) Estimates of snow density for sites A, B and C, plotted in order left to right. (Bottom) Estimates of surface mass balance corresponding to the above estimates of snow density and ice-penetrating radar signals.

region suggests changes in atmospheric moisture transport are the dominant driver of the observed SMB trends.

6. Conclusions and future work. We have presented a novel class of spatial models for monotone curve estimation. For these data we constructed this model through kernel convolutions that enables prediction of snow density below observed depths and at locations where snow cores have not been drilled. Using 19-fold cross-validation, we selected a weighted spatially-varying generalized linear model using M-spline bases for the kernel convolution, where the coefficients of the integrated kernels are modeled using independent log-Gaussian processes. We have demonstrated how this model estimates snow density below observed

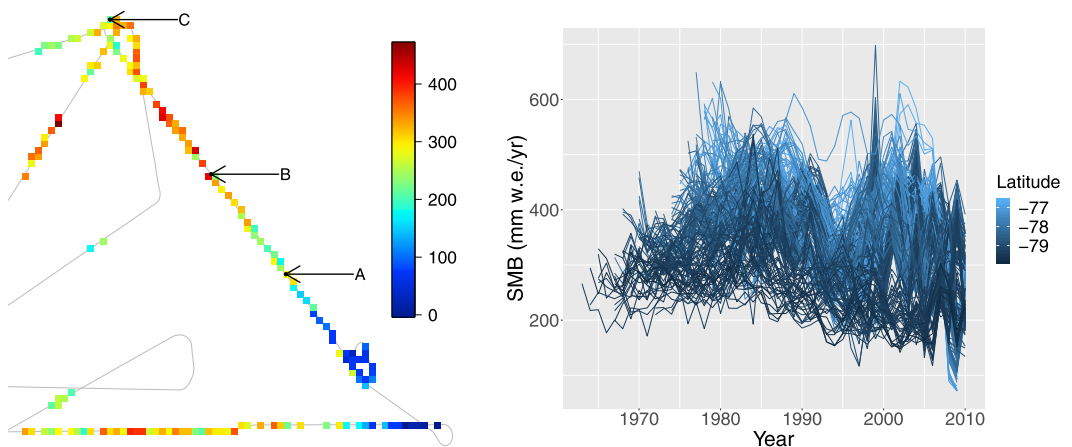


FIG. 7. (Left) Estimated mean SMB (mm w.e./yr), averaged over all years (Right) Estimated mean SMB over all years, colored by latitude.

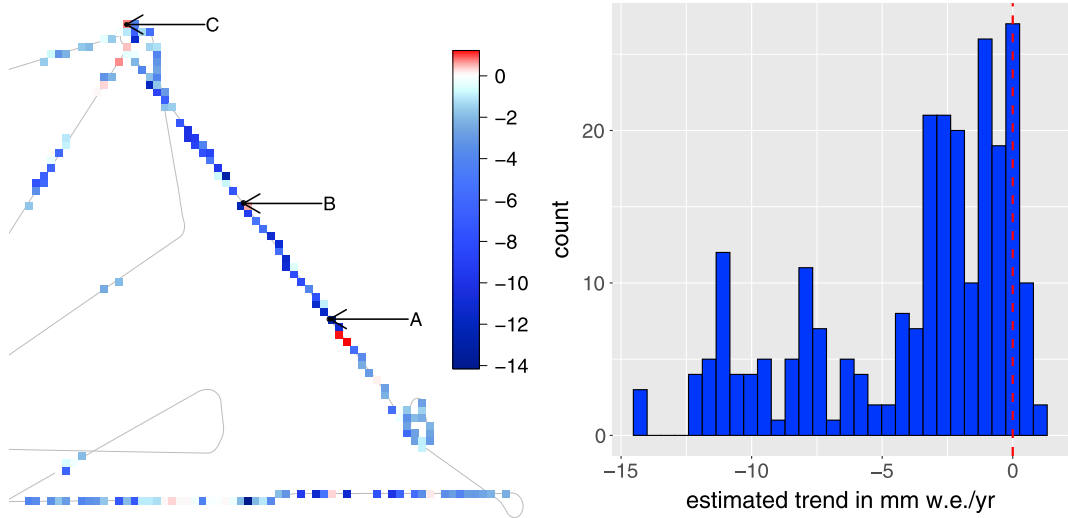


FIG. 8. *Estimated trend in mean SMB (mm w.e./yr) (Left) plotted by location and (Right) in histogram with red vertical line at 0.*

levels and where no data has been acquired. Using these snow density estimates, we have estimated surface mass balance over the recent past and find generally negative trends in SMB over the West Antarctic Ice Sheets.

In this analysis we did not account for the time of density measurement. In future work we will account for time differences between the time of radar measurement and the snow core drilling through a spatiotemporal model. However, the demonstrated ability to interpolate snow densification rates has several applications relevant to the cryospheric community. As demonstrated, the extension of density profiles to arbitrary spatial locations is useful in estimating local annual SMB using ice-penetrating radar, greatly expanding the spatial density and coverage of these measurements over traditional coring techniques. Similarly, quantifying the total mass loss in Antarctica and similar regions is a primary target within the community, with critical implications for sea-level rise (IPCC (2013)). A primary method for determining net mass loss uses laser altimetry to measure changes in ice sheet surface elevation but also requires accurate estimates of snow density to estimate mass changes (Li and Zwally (2011)). The laser altimetry method, in particular, is a focus of several national and international laboratories and organizations, highlighted by NASA's recent ICESat-2 satellite launch in 2018 and the ongoing ESA CryoSat-2 laser altimeter mission (Tedesco et al. (2014)). Lastly, to improve snow density estimation, we will consider extensions of White et al. (2019), where we consider sites that would sequentially minimize integrated error criteria over regions of Antarctica.

A natural extension of our proposed framework could increase the number of knots included in the MISP and provide shrinkage on the integrated kernel coefficients through an autoregressive prior distribution (see Lang and Brezger (2004)). This approach would likely reduce the model's sensitivity to knot selection. More importantly, this extension would enable the automation of this approach for other applications.

Acknowledgments. We thank the three anonymous reviewers as well as the Editor for their comments that have helped improve the manuscript.

Funding. Summer Rupper acknowledges funding from NASA grant NNX16AJ72G.

SUPPLEMENTARY MATERIAL

Supplement to “Hierarchical integrated spatial process modeling of monotone West Antarctic snow density curves” (DOI: [10.1214/21-AOAS1443SUPPA](https://doi.org/10.1214/21-AOAS1443SUPPA); .zip). We provide data and code to obtain final model results.

Supplement to “Hierarchical integrated spatial process modeling of monotone West Antarctic snow density curves” (DOI: [10.1214/21-AOAS1443SUPPB](https://doi.org/10.1214/21-AOAS1443SUPPB); .pdf). We explore covariance of the MISP model, detail M- and I-spline basis functions, present detailed model comparison, and give extended model fitting results.

REFERENCES

- ALBERT, M., SHUMAN, C., COURVILLE, Z., BAUER, R., FAHNSTOCK, M. and SCAMBOS, T. (2004). Extreme firn metamorphism: Impact of decades of vapor transport on near-surface firn at a low-accumulation glazed site on the East Antarctic plateau. *Annals of Glaciology* **39** 73–78.
- ALLEY, R. B., SALTZMAN, E. S., CUFFEY, K. M. and FITZPATRICK, J. J. (1990). Summertime formation of Depth Hoar in central Greenland. *Geophys. Res. Lett.* **17** 2393–2396.
- BANTA, J. R., MCCONNELL, J. R., FREY, M. M., BALES, R. C. and TAYLOR, K. (2008). Spatial and temporal variability in snow accumulation at the West Antarctic ice sheet divide over recent centuries. *J. Geophys. Res., Atmos.* **113** D23102.
- BARLOW, R. E., BARTHOLOMEW, D. J., BREMNER, J. M. and BRUNK, H. D. (1972). *Statistical Inference Under Order Restrictions*. Wiley, New York.
- BROMWICH, D. H., NICOLAS, J. P., MONAGHAN, A. J., LAZZARA, M. A., KELLER, L. M., WEIDNER, G. A. and WILSON, A. B. (2013). Central West Antarctica among the most rapidly warming regions on Earth. *Nat. Geosci.* **6** 139–145.
- BROWN, T. A. (1974). Admissible scoring systems for continuous distributions. Technical Report No. P-5235, The Rand Corporation, Santa Monica, California.
- BURGENER, L., RUPPER, S., KOENIG, L., FORSTER, R., CHRISTENSEN, W. F., WILLIAMS, J., KOUTNIK, M., MIEGE, C., STEIG, E. J. et al. (2013). An observed negative trend in West Antarctic accumulation rates from 1975 to 2010: Evidence from new observed and simulated records. *J. Geophys. Res., Atmos.* **118** 4205–4216.
- CARPENTER, B., GELMAN, A., HOFFMAN, M. D., LEE, D., GOODRICH, B., BETANCOURT, M., BRUBAKER, M., GUO, J., LI, P. et al. (2017). Stan: A probabilistic programming language. *J. Stat. Softw.* **76**.
- CUFFEY, K. M. and PATERSON, W. S. B. (2010). *The Physics of Glaciers*. Academic Press, San Diego.
- EISEN, O., FREZZOTTI, M., GENTHON, C., ISAKSSON, E., MAGAND, O., VAN DEN BROEKE, M. R., DIXON, D. A., EKAYKIN, A., HOLMLUND, P. et al. (2008). Ground-based measurements of spatial and temporal variability of snow accumulation in East Antarctica. *Reviews of Geophysics* **46** RG2001.
- FRYER, M. (1976). Some errors associated with the non-parametric estimation of density functions. *IMA J. Appl. Math.* **18** 371–380.
- FUJITA, S., MAENO, H., URATSUKA, S., FURUKAWA, T., MAE, S., FUJII, Y. and WATANABE, O. (1999). Nature of radio echo layering in the Antarctic ice sheet detected by a two-frequency experiment. *J. Geophys. Res., Solid Earth* **104** 13013–13024.
- GELFAND, A. E. and KUO, L. (1991). Nonparametric Bayesian bioassay including ordered polytomous response. *Biometrika* **78** 657–666. [MR1130934 https://doi.org/10.1093/biomet/78.3.657](https://doi.org/10.1093/biomet/78.3.657)
- GELFAND, A. E., KIM, H.-J., SIRMANS, C. F. and BANERJEE, S. (2003). Spatial modeling with spatially varying coefficient processes. *J. Amer. Statist. Assoc.* **98** 387–396. [MR1995715 https://doi.org/10.1198/016214503000170](https://doi.org/10.1198/016214503000170)
- GNEITING, T. and RAFTERY, A. E. (2007). Strictly proper scoring rules, prediction, and estimation. *J. Amer. Statist. Assoc.* **102** 359–378. [MR2345548 https://doi.org/10.1198/01621450600001437](https://doi.org/10.1198/01621450600001437)
- HEFLEY, T. J., BROMS, K. M., BROST, B. M., BUDERMAN, F. E., KAY, S. L., SCHARF, H. R., TIPTON, J. R., WILLIAMS, P. J. and HOOTEN, M. B. (2017). The basis function approach for modeling autocorrelation in ecological data. *Ecology* **98** 632–646. <https://doi.org/10.1002/ecy.1674>
- HERRON, M. M. and LANGWAY, C. C. (1980). Firn densification: An empirical model. *Journal of Glaciology* **25** 373–385.
- HIGDON, D. (1998). A process-convolution approach to modelling temperatures in the North Atlantic Ocean. *Environ. Ecol. Stat.* **5** 173–190.
- HIGDON, D. (2002). Space and space–time modeling using process convolutions. In *Quantitative Methods for Current Environmental Issues* 37–56. Springer, London. [MR2059819](https://doi.org/10.1007/978-1-4020-0598-1_3)

- HÖRHOOLD, M. W., KIPFSTUHL, S., WILHELMS, F., FREITAG, J. and FRENZEL, A. (2011). The densification of layered polar firn. *J. Geophys. Res., Earth Surf.* **116**.
- IPCC (2013). *Climate Change 2013: The Physical Science Basis. Contribution of Working Group I to the Fifth Assessment Report of the Intergovernmental Panel on Climate Change.* Cambridge Univ. Press, Cambridge, United Kingdom and New York, NY, USA.
- KEELER, D. G., RUPPER, S. B., FORSTER, R. and MIÈGE, C. (2020). A probabilistic automated isochrone picking routine to derive annual surface mass balance from radar echograms. *IEEE Trans. Geosci. Remote Sens.*
- KOENIG, L., FORSTER, R., BRUCKER, L. and MILLER, J. (2014). Remote sensing of accumulation over the Greenland and Antarctic ice sheets. In *Remote Sensing of the Cryosphere* 157–186. Wiley-Blackwell, New York.
- KRÜGER, F., LERCH, S., THORARINSDOTTIR, T. L. and GNEITING, T. (2020). Predictive inference based on Markov chain Monte Carlo output. *Int. Stat. Rev.*
- LAMOREY, G. and COOPER, T. (2002). Siple dome WAISCORES density data for shallow cores.
- LANG, S. and BREZGER, A. (2004). Bayesian P-splines. *J. Comput. Graph. Statist.* **13** 183–212. [MR2044877 https://doi.org/10.1198/1061860043010](https://doi.org/10.1198/1061860043010)
- LENAERTS, J. T. M., VAN DEN BROEKE, M. R., VAN DE BERG, W. J., VAN MEIJAARD, E. and MUNNEKE, P. K. (2012). A new, high-resolution surface mass balance map of Antarctica (1979–2010) based on regional atmospheric climate modeling. *Geophys. Res. Lett.* **39** L04501.
- LI, J. and ZWALLY, H. J. (2011). Modeling of firn compaction for estimating ice-sheet mass change from observed ice-sheet elevation change. *Annals of Glaciology* **52** 1–7.
- LIN, L. and DUNSON, D. B. (2014). Bayesian monotone regression using Gaussian process projection. *Biometrika* **101** 303–317. [MR3215349 https://doi.org/10.1093/biomet/ast063](https://doi.org/10.1093/biomet/ast063)
- MARRON, J. S. and WAND, M. P. (1992). Exact mean integrated squared error. *Ann. Statist.* **20** 712–736. [MR1165589 https://doi.org/10.1214/aos/1176348653](https://doi.org/10.1214/aos/1176348653)
- MATHESON, J. E. and WINKLER, R. L. (1976). Scoring rules for continuous probability distributions. *Manage. Sci.* **22** 1087–1096.
- MAYEWSKI, P. A., FREZZOTTI, M., BERTLER, N., OMMEN, T. V., HAMILTON, G., JACKA, T. H., WELCH, B., FREY, M., DAHE, Q. et al. (2005). The international trans-Antarctic scientific expedition (ITASE): An overview. *Annals of Glaciology* **41** 180–185.
- MEDLEY, B., JOUGHIN, I., SMITH, B. E., DAS, S. B., STEIG, E. J., CONWAY, H., GOGINENI, S., LEWIS, C., CRISCITIELLO, A. S. et al. (2014). Constraining the recent mass balance of pine island and thwaites glaciers, West Antarctica, with airborne observations of snow accumulation. *Cryosphere* **8** 1375–1392.
- MEYER, M. C. (2008). Inference using shape-restricted regression splines. *Ann. Appl. Stat.* **2** 1013–1033. [MR2516802 https://doi.org/10.1214/08-AOAS167](https://doi.org/10.1214/08-AOAS167)
- MIÈGE, C., FORSTER, R. R., BOX, J. E., BURGESS, E. W., MCCONNELL, J. R., PASTERIS, D. R. and SPIKES, V. B. (2013). Southeast Greenland high accumulation rates derived from firn cores and ground-penetrating radar. *Annals of Glaciology* **54** 322–332.
- MÜLLER, H.-G. and SCHMITT, T. (1988). Kernel and probit estimates in quantal bioassay. *J. Amer. Statist. Assoc.* **83** 750–759. [MR0963803](https://doi.org/10.1080/01621459.1988.10510633)
- NEELON, B. and DUNSON, D. B. (2004). Bayesian isotonic regression and trend analysis. *Biometrics* **60** 398–406. [MR2066274 https://doi.org/10.1111/j.0006-341X.2004.00184.x](https://doi.org/10.1111/j.0006-341X.2004.00184.x)
- PADEN, J., LI, J., LEUSCHEN, C., RODRIGUEZ-MORALES, F. and HALE, R. (2019). IceBridge snow radar L1B geolocated radar echo strength profiles, Version 2.
- RAMSAY, J. O. (1988). Monotone regression splines in action. *Statist. Sci.* **3** 425–441.
- RIIHIMÄKI, J. and VEHTARI, A. (2010). Gaussian processes with monotonicity information. In *Proceedings of the Thirteenth International Conference on Artificial Intelligence and Statistics* 645–652.
- ROBERTSON, T., WRIGHT, F. T. and DYKSTRA, R. L. (1988). *Order Restricted Statistical Inference.* Wiley Series in Probability and Mathematical Statistics: Probability and Mathematical Statistics. Wiley, Chichester. [MR0961262](https://doi.org/10.1002/978-1-4612-4024-2)
- TANNER, M. A. (1996). *Tools for Statistical Inference: Methods for the Exploration of Posterior Distributions and Likelihood Functions.* 3rd ed. Springer Series in Statistics. Springer, New York. [MR1396311 https://doi.org/10.1007/978-1-4612-4024-2](https://doi.org/10.1007/978-1-4612-4024-2)
- TEDESCO, M., PARRINELLO, T., WEBB, C. and MARKUS, T. (2014). Remote sensing missions and the cryosphere. In *Remote Sensing of the Cryosphere* 382–392. Wiley, New York.
- VERJANS, V., LEESON, A. A., NEMETH, C., STEVENS, C. M., KUIPERS MUNNEKE, P., NOËL, B. and WESSEM, J. M. V. (2020). Bayesian calibration of firn densification models. *Cryosphere Discuss.* 1–23.
- WHITE, P., KEELER, D. and RUPPER, S. (2021). Supplement to “Hierarchical integrated spatial process modeling of monotone West Antarctic snow density curves.” <https://doi.org/10.1214/21-AOAS1443SUPPA>, <https://doi.org/10.1214/21-AOAS1443SUPPB>

- WHITE, P. A., REESE, C. S., CHRISTENSEN, W. F. and RUPPER, S. (2019). A model for Antarctic surface mass balance and ice core site selection. *Environmetrics* **30** e2579, 19. MR4039225 <https://doi.org/10.1002/env.2579>
- WHITE, P., KEELER, D., SHEANSHANG, D. and RUPPER, S. (2020). Improving interpretable piecewise linear models through hierarchical spatial and functional smoothing. Preprint. Available at [arXiv:2006.09329](https://arxiv.org/abs/2006.09329).